Journal of Nanobiotechnology

RESEARCH

Open Access

Injectable biocompatible nanocomposites of Prussian blue nanoparticles and bacterial cellulose as a safe and effective photothermal cancer therapy

Hwichan Hong[1†], MinKyu Kim[1†], Wooseung Lee[1], Miyeon Jeon[1], Chaedong Lee[1], Hoonsub Kim[1], Hyung-Jun Im[1,2,3,4,5*] and Yuanzhe Piao[1,4,5*]

Abstract

Photothermal therapy (PTT) is a novel cancer treatment using a photoabsorber to cause hyperthermia to kill tumors by laser irradiation. Prussian blue nanoparticles (PB NPs) are considered as next-generation photothermal agents due to the facile synthesis and excellent absorption of near-infrared light. Although PB NPs demonstrate remarkable PTT capabilities, their clinical application is limited due to their systemic toxicity. Bacterial cellulose (BC) has been applied to various bio-applications based on its unique properties and biocompatibility. Herein, we design composites with PB NPs and BC as an injectable, highly biocompatible PTT agent (IBC-PB composites). Injectable bacterial cellulose (IBC) is produced through the trituration of BC, with PB NPs synthesized on the IBC surface to prepare IBC-PB composites. IBC-PB composites show in vitro and in vivo photothermal therapeutic effects similar to those of PB NPs but with significantly greater biocompatibility. Specifically, in vitro therapeutic index of IBC-PB composites is 26.5-fold higher than that of PB NPs. Furthermore, unlike PB NPs, IBC-PB composites exhibit no overt toxicity in mice as assessed by blood biochemical analysis and histological images. Hence, it is worth pursuing further research and development of IBC-PB composites as they hold promise as safe and efficacious PTT agents for clinical application.

Keywords Prussian blue nanoparticles, Bacterial celluloses, Nanocomposites, Photothermal therapy, Improved biocompatibility

†Hwichan Hong and MinKyu Kim contributed equally to this work.

*Correspondence:
Hyung-Jun Im
iiihjjj@gmail.com
Yuanzhe Piao
parkat9@snu.ac.kr
Full list of author information is available at the end of the article

Graphical Abstract

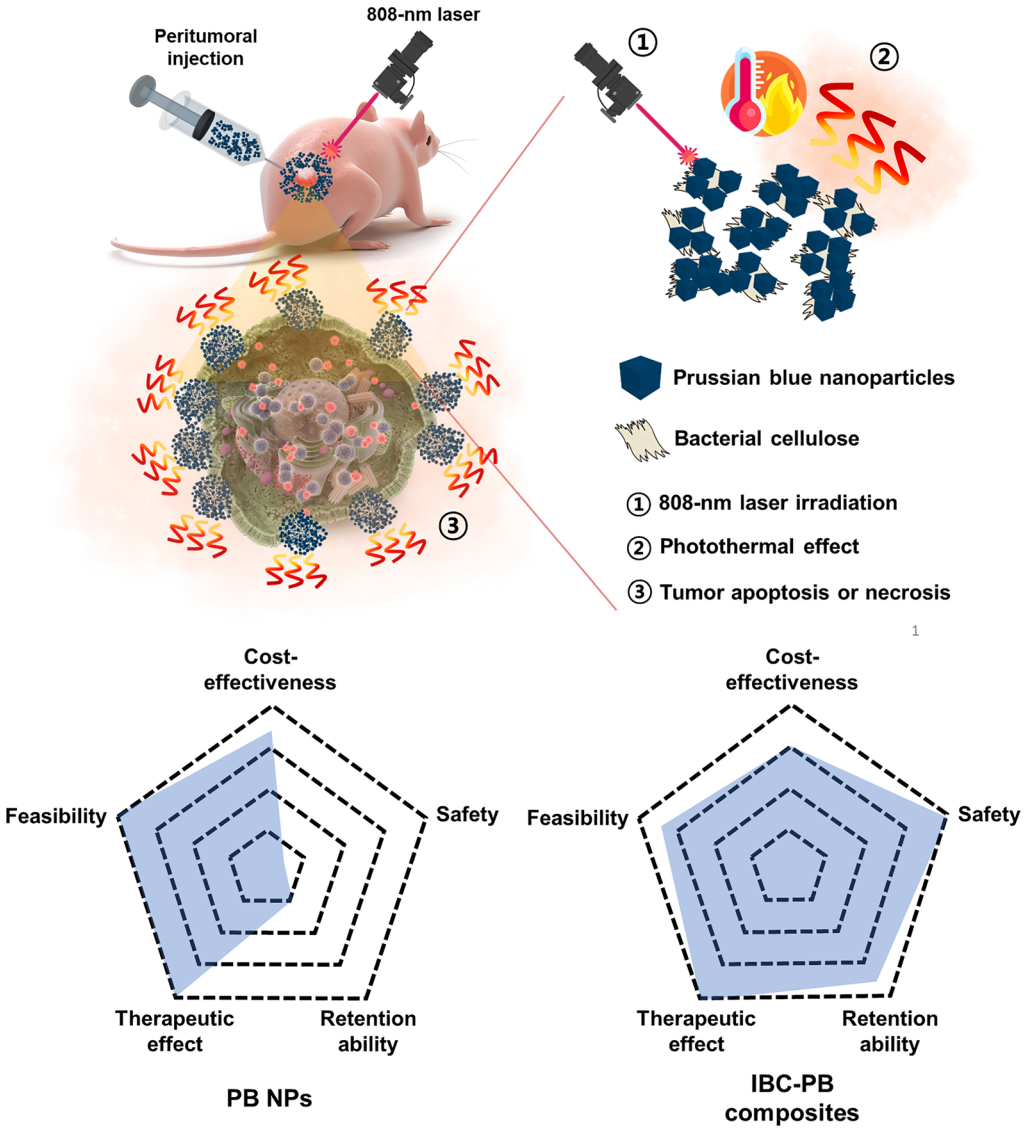

Introduction

Photothermal therapy (PTT) is an emerging cancer treatment strategy that has been extensively researched in recent years [1–4]. This method involves the use of near-infrared (NIR) laser to irradiate photothermal agents accumulated in cancer lesions. These agents then convert the absorbed light into heat, causing a rise in local tissue temperature and thereby causing apoptosis or necrosis of tumor cells [5–8]. Numerous materials, including carbon-based materials [9, 10], gold [11–13], silver [14–16], iron oxide [17, 18], and germanium nanocrystals [19, 20], are currently being developed as potential agents for PTT. Also, a recent phase 1 clinical trial in patients with prostate cancer demonstrated the feasibility of PTT using a gold nanoshell, with successful tumor ablation and no serious complications observed in 94% (15/16) of patients [21]. This study demonstrates the promise of PTT agents for clinical applications, but the high cost of gold nanoparticles is considered as a potential limitation hindering large-scale clinical trials [22].

Prussian blue (PB) is an ancient low-cost dye that can be easily prepared [23]. Due to its strong optical absorbance in the NIR region and good photostability, Prussian blue nanoparticles (PB NPs) have been developed

as potential photothermal agents for cancer [24–26]. PB NPs have gained significant attention in the biomedical field primarily due to their facile synthesis, which allows for rapid and efficient production. Their controllable size and shape, coupled with the ease of surface modification, offer multifunctionality, making them ideal for a range of applications like theranostics and drug delivery. Additionally, their cost-effectiveness ensures that they remain an attractive option for researchers and practitioners looking for budget-friendly yet effective solutions [27–30]. In practice, the United States Food and Drug Administration (US FDA) approved PB NPs as a clinical medicine for oral administration to treat patients with internal contamination of thallium (Tl^+) or radiocesium (Cs^+) poisoning in 2003 [30]. However, PB NPs have disadvantages as well, such as the accumulation in normal organs when they are systemically administered [31]. In particular, Chen et al. reported that intravenously injected PB NPs in mice caused acute liver injury, an outcome attributed to the substantial accumulation of the nanoparticles in Kupffer cells, the resident macrophages in the liver [32].

Bacterial cellulose (BC) stands out in the realm of biomaterials due to its exceptional biocompatibility, allowing it to be used in biological systems without causing adverse reactions. BC's inherent flexibility means it can conform to various shapes and structures, making it especially useful in situations that demand adaptability, such as molds or dynamic biomedical environments. The porous nature of BC not only provides it with a lightweight structure but also allows for efficient delivery and retention of bioactive agents, further establishing its potential in drug delivery systems and tissue engineering scaffolds. Based on these properties, BC is used in various biomedical applications, such as diagnostic sensors [33, 34], tissue engineering [35], drug delivery systems [36–38], wound dressing [39–42], and artificial skin [43]. Nata de coco, a type of BC invented in 1949, is made by fermenting coconut water through Komagataeibacter xylinus [44]. Bacterial cellulose can be used by itself, but it is also used to make composites with various additives such as biopolymers [45, 46], quantum dots [47, 48], nanoparticles [39, 40, 49, 50] and nano carbons [51, 52]. Nanocellulose reportedly has an excellent stabilizing effect for metal nanoparticles, which can promote the nucleation of nanoparticles as well as prevent their agglomeration [53]. Therefore, we hypothesized that BC could be used to stabilize PB and reduce its the toxicity.

Herein, we successfully manufactured and synthesized a composite of injectable bacterial cellulose with PB NPs that is biocompatible, locally injectable, and is amenable with repeated PTT sessions. The injectable BC composite with PB NPs (IBC-PB composites) went through a simple reduction reaction. The PB NPs were directly grown onto BC fragmented on the nanoscale. We hypothesized that IBC-PB composites can exert a potent PTT effect while remaining less toxic compared to PB NPs due to the biocompatibility of BC and the enhanced stability realized here.

Results and discussion

Injectable bacterial cellulose (IBC) synthesis from nata de coco

Nata de coco is purified by flowing deionized water (D.W.) for several days to remove impurities such as remaining bacteria and sugar. After purification, physical grinding and lyophilization were conducted for an accurate quantitative experiment. Schweitzer's reagent was used to reduce the nanofiber structure of BC to obtain an injectable bacterial cellulose. After the pre-treatment, the injectable quantified bacterial cellulose was successfully obtained (Additional file 1: Fig S1).

Synthesis of PB NPs and IBC-PB composites

For the PB and IBC-PB composites, they were simply synthesized by the reduction of $K_3[Fe(CN)_6]$ under an acidic condition at 80 ℃ with the addition of Polyvinylpyrrolidone (PVP) or IBC. The synthesized IBC-PB composites were dispersed at 50 ml D.W. and kept in a refrigerator at 5 ℃ to prevent contamination (Fig. 1).

Characterizations of the PB NPs and IBC-PB composites

The morphology of IBC-PB composites were examined by scanning electron microscope (SEM), and PB NPs

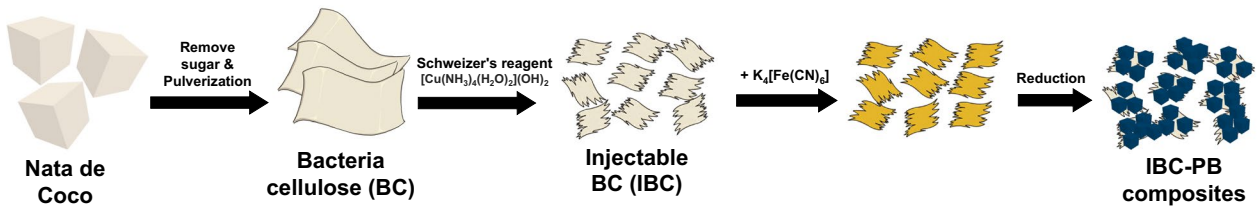

Fig. 1 Schematic diagram of the IBC-PB composites synthesis procedure

with a cubic structure were found to be evenly distributed on the IBC sheet (Fig. 2a–d). The ratio of PB NPs per area and particle size increases according to the concentration of potassium ferricyanide (0.25, 0.5, 0.75, and 1 mmol respectively). The PB NP size of the IBC-PB composites were 150–275 nm, and we synthesized 200 nm PB NPs as a control (Additional file 1: Fig S2). Pristine PB NPs were utilized as a control in all further in vitro and in vivo studies.

TGA analysis was conducted under an air condition to measure the volume of PB nanoparticles (Fig. 2e). From the results of the TGA analysis of BC, only 0.8% of the current weight of cellulose remained after calcination at a temperature that exceeded 600 ℃, implying that all cellulose was removed at this high temperature. According to this result, the remaining important material of IBC-PB composites after TGA was confirmed to be iron oxide, which was produced by the calcination of PB, with the level proportional to the amount of potassium ferricyanide from 0 to 1 mmol.

The XRD patterns of PB and IBC-PB composites are matched with that of a face-centered cubic lattice and are in good agreement with the standard data of PB (ICDD PDF2 01-073-0687). The peaks at 2-theta values of 17.4, 24.7, 35.1, 39,4, 43.5, 50.8, 54.1 and 57.3° can be assigned correspondingly to the (200), (220), (400), (420), (422), (440), (600) and (620) planes of the PB (Fig. 2f).

The FT-IR spectroscopy displayed a characteristic peak of CN stretching at 2085 cm^{-1}, O-H around 3300 cm^{-1}, C-O-C stretches at 1050 m^{-1} (Additional file 1: Fig S3).

SEM, XRD, TGA, FT-IR data showed that Prussian blue nanoparticles were synthesized proportionally to the amount of the initial PB precursor and were uniformly distributed on the BC sheet.

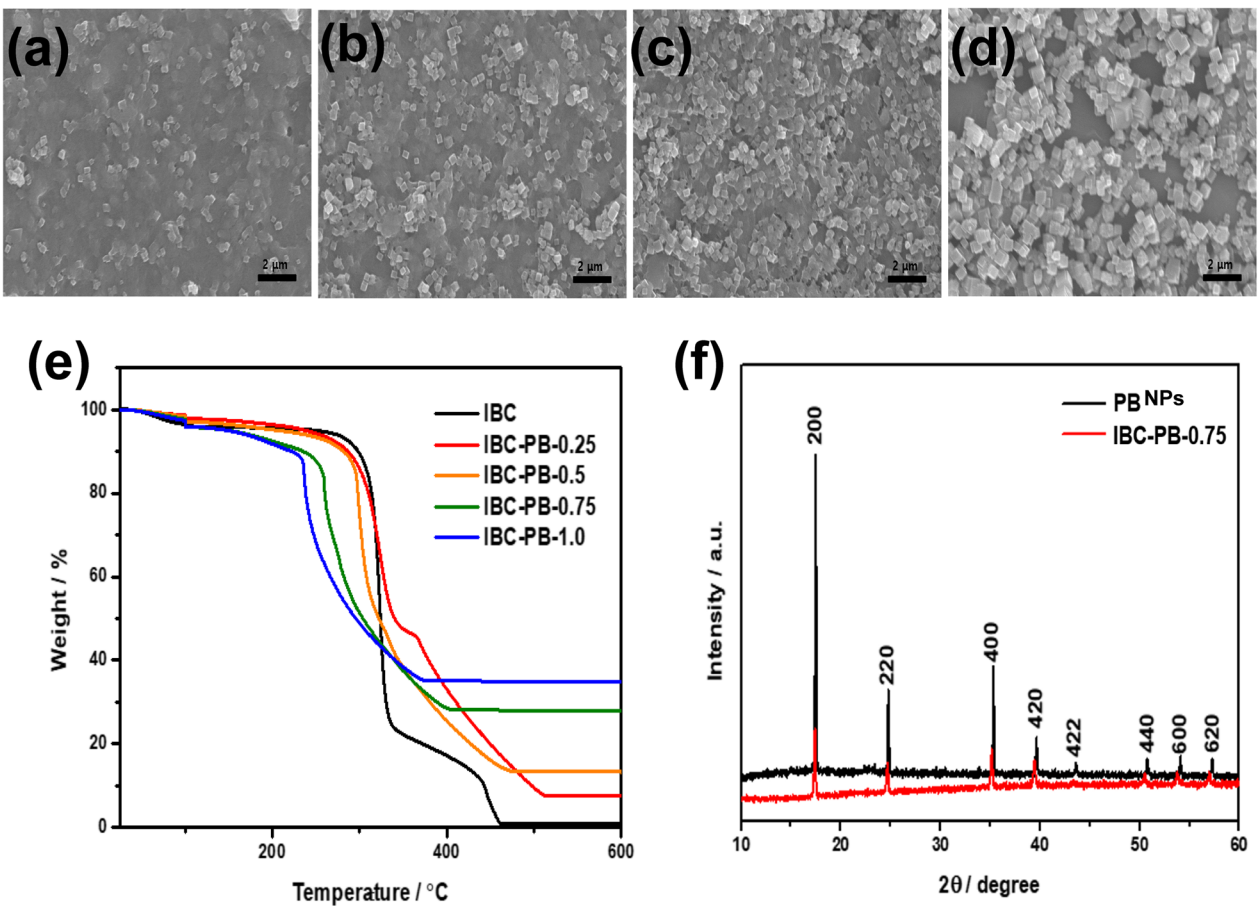

Fig. 2 Characterization of the IBC-PB composites: (a-d) SEM images of an IBC-PB composites according to the $K_4[Fe(CN)_6]$ concentration gradient (left to right: (**a**) 0.25, (**b**) 0.5, (**c**) 0.75, and (**d**) 1 mmol of $K_4[Fe(CN)_6]$). **e** Thermogravimetric analysis (TGA) of an IBC-PB composites according to the $K_4[Fe(CN)_6]$ concentration gradient (0, 0.25, 0.5, 0.75, and 1 mmol of $K_4[Fe(CN)_6]$). **f** X-ray diffraction (XRD) pattern data of PB NPs and IBC-PB composites. (*IBC-PB* IBC-PB composites)

Photothermal effect of the IBC-PB composites

The absorbance spectra of the IBC-PB composites according to a UV–visible spectrometer showed absorption bands at 600–900 nm with a high peak value at 800–900 nm. Due to its strong NIR absorption, IBC-PB composites had noticeable photothermal effects. The absorbance intensity increased in a linearly proportional manner relative to the initial concentration of potassium ferricyanide from 0.25 to 0.75 mmol. The absorbance of the IBC-PB composites (1 mmol) was mostly in accord with IBC-PB composites (0.75 mmol), allowing us to confirm that saturation accrued at 0.75 mmol (Fig. 3a).

During the photothermal test, the temperature of the IBC-PB composites in each case was increased by irradiation using an 808 nm-laser with at an intensity level of 1 W cm^{-2} by 20.5 ℃ in 5 min (Fig. 3b). The photothermal effect of IBC-PB composites increased with the amount of PB from 0.25 to 0.75 mmol, with the results for IBC-PB composites (1 mmol) in good agreement with those of IBC-PB composites (0.75 mmol). This is consistent with the UV–vis spectra data, where the photothermal effect was saturated at 0.75 mmol of $K_4[Fe(CN)_6]$. Therefore, IBC-PB composites (0.75 mmol) was selected as the leading group for all further in vitro and in vivo studies.

Repetitive photothermal ability of IBC-PB composites

In the repetition demonstration, the laser was irradiated five times for five minutes and the temperature rise was maintained by 25 ℃. As a result, the photothermal effect of IBC-PB composites was maintained after multiple laser irradiation trials (Fig. 3c). After five cycles, the UV–vis spectra confirmed that the absorbance at NIR was maintained (Fig. 3d).

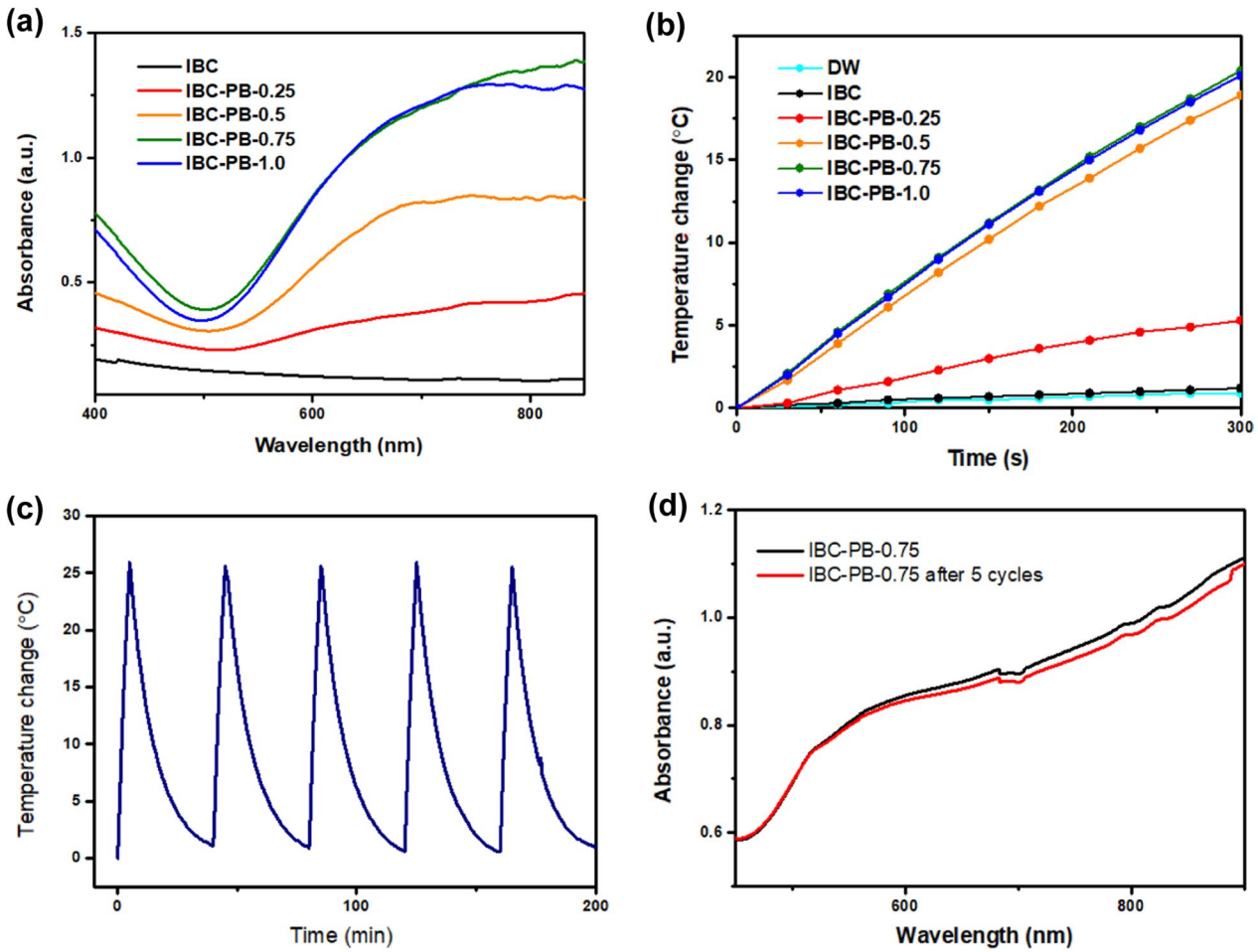

Fig. 3 Photothermal characterization of the IBC-PB composites: (**a**) absorbance spectra scanning and (**b**) photothermal effect of the IBC-PB composites in the series of $K_4[Fe(CN)_6]$ concentrations (0, 0.25, 0.5, 0.75, and 1 mmol of $K_4[Fe(CN)_6]$ at an intensity level of 1 W cm^{-2} for five minutes. **c** Validation of the photothermal ability of the IBC-PB composites during five cycles of laser irradiation at an intensity level of 1 W cm^{-2} for 200 min. **d** Absorbance spectra comparison of IBC-PB composites with 0.75 mmol of $K_4[Fe(CN)_6]$ before and after five repeated laser irradiation cycles. (*IBC-PB* IBC-PB composites)

In vitro photothermal therapeutic effect in the 4T1 breast cancer cell line

The in vitro PTT effects of the BC, PB NPs and IBC-PB composites were evaluated using an 808 nm NIR laser (Fig. 4a). BC had no overt cytotoxicity with or without laser irradiation (Fig. 4b). The unirradiated IBC-PB composites showed no cytotoxicity at all treated concentrations. The laser-irradiated IBC-PB composites showed a dramatic photothermal therapeutic effect with more than 82% cell killing ability from a PB concentration of 20 μg 200 μL^{-1} (Fig. 4d). Live 4T1 cells were scarcely observed after in vitro PTT at PB concentrations above 20 μg 200 μL^{-1} in the IBC-PB composites. However, the cells were intact in the IBC-PB composites without PTT (Fig. 4e). On the other hand, despite the fact that the PB NPs displayed a high PTT effect of more than 80% cell death when irradiated by an 808 nm laser at a concentration of 20 μg 200 μL^{-1}, the unirradiated PB NPs also exhibited increased cytotoxicity as their concentration was increased. This suggests that cell death was caused not only by the PTT effect but also by the inherent cytotoxicity of the PB NPs (Fig. 4c).

In vivo retention at the tumor region of PB NPs and IBC-PB composites

We also conducted an in vivo PTT experiment with 4T1 tumor-bearing mice. We injected PB NPs and IBC-PB composites peritumorally as earlier studies reported that doing so resulted in better positioning and an improved PTT effect compared to an intratumoral injection [30, 56]. We compared the retention profiles of the PB NPs and the IBC-PB composites after a peritumoral injection around the subcutaneously located 4T1 tumor tissue region with 4T1 tumor-bearing mice (n = 3) for seven days (Additional file 1: Fig S4). The peritumoral injections of the PB NPs and IBC-PB composites were clearly visible around the tumor region immediately after the injection (day 0). However, the PB NPs rapidly disappeared and were difficult to detect 24 h post-injection due to systemic absorption and were not visible in the resected tumor images seven days after the injection. In contrast, the IBC-PB composites remained at the site of the injection up to seven days post-injection, as evidenced by images taken of resected tumors. It should be noted that the IBC-PB composites were not fully absorbed by the body, suggesting that the IBC-PB composites could be repeatedly targeted by an 808 nm laser for complete tumor removal via repeatable PTT and that they can also be considered more biocompatible than PB NPs.

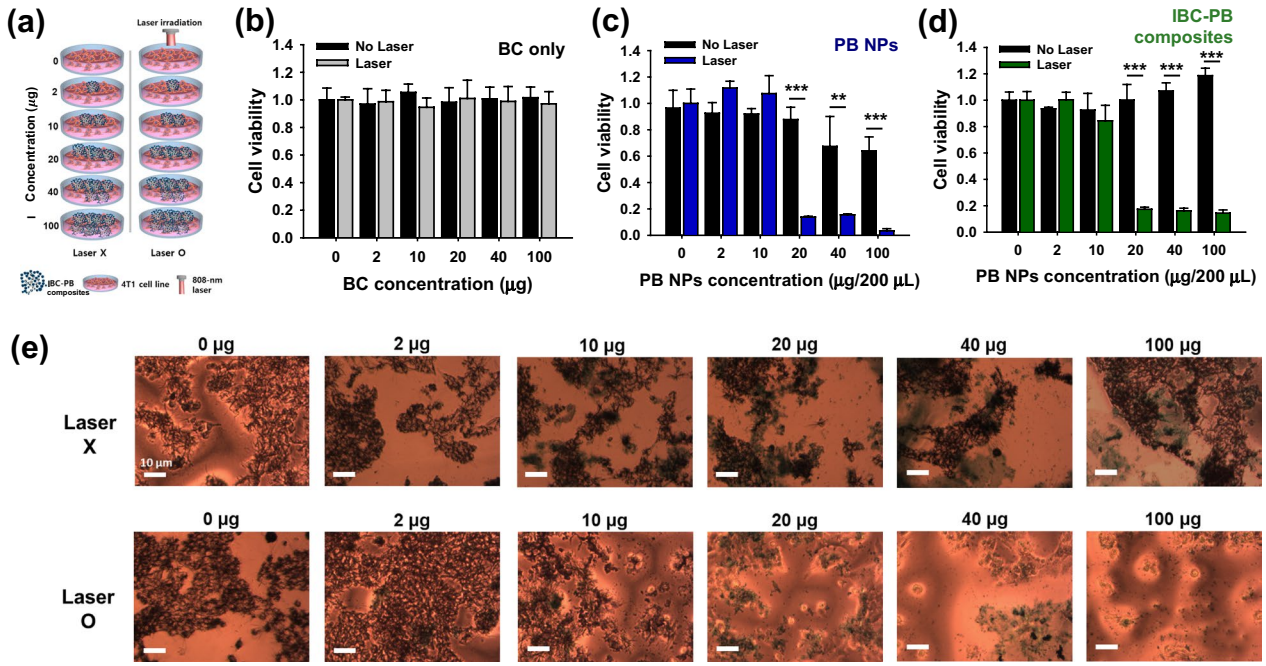

Fig. 4 In vitro PTT effect study: (**a**) experimental design of in vitro PTT in the 4T1 breast cancer cell line. In vitro PTT effect (808 nm, 2 W cm^{-2}, 5 min) according to the concentration gradient (0, 2, 10, 20, 40, 100 μg 200 μL^{-1}) of (**b**) IBC, (**c**) PB NPs, and (**d**) IBC-PB composites (n = 3, mean ± s.d.). **e** Optical images of cell populations treated with the series of IBC-PB composites with and without PTT. *: $P < 0.05$, **: $P < 0.01$, ***: $P < 0.001$. The statistical analysis was conducted by means of student's t test for b, c, and d

Peritumoral injection provides a notable advantage by improving the precise delivery of treatment to the tumor location, while reducing the risk of adverse effects on the entire body [54–56]. Furthermore, the combination of this method with the immunotherapy shows potential for positive outcomes, even when dealing with metastatic cancers (Fig. 5) [57, 58].

In vivo photothermal imaging and therapy in 4T1 cancer-bearing mice

For the in vivo photothermal imaging and therapy, normal saline (NS), PB NPs, and IBC-PB composites were peritumorally injected into 4T1 tumor bearing mice. After the injection in each group, an 808 nm NIR laser was irradiated under the condition of 2 W cm^{-2} for five minutes only once. The three different injected materials were separated into two groups, referred to the laser irradiated and unirradiated groups (NS, PB NPs, IBC-PB composites, NS + Laser, PB NPs + Laser, and IBC-PB composites + Laser). In vivo photothermal imaging was conducted and the temperature distribution at the tumor sites was observed (Fig. 6a). The temperature at the NS-injected tumor area increased by only 6.2 °C from 32.7 to 38.9 °C after 808-nm laser irradiation. In contrast, the temperature in the tumors injected with PB NPs and IBC-PB composites increased dramatically, reaching 47.7 °C (ΔT: 16.2 °C) and 48.1 °C (ΔT: 20.4 °C), respectively. The IBC-PB composites showed a slightly larger temperature change of 4.2 °C compared to that of the PB NPs (Fig. 6b, c). This demonstrates that the IBC-PB composites has a potent photothermal effect in vivo.

The tumor tissue growth in the unirradiated groups and the NS + laser group increased proportionally with time. In contrast, the PB + Laser and IBC-PB composites + Laser groups showed significantly smaller tumor sizes compared to the control groups (NS, PB NPs, and IBC-PB composites) ($P < 0.05$ for all comparisons at day 18) (Fig. 6d). The suppressed tumor growth was evaluated by examining the tumor volume up to 18 days (Fig. 6e). The IBC-PB composites showed a 71.5% tumor growth suppression rate, demonstrating greater tumor-growth inhibition ability compared to the control groups, particularly the PB NPs (68.5% tumor-growth suppression effect). The body weight up to 18 days after treatment was not significantly reduced in all groups (Fig. 6f).

In vitro cytotoxicity test in the RAW 264.7 macrophage cell line

Given the limitations in the toxicity of PB NPs, we undertook a further evaluation of the toxicity profiles of both the PB NPs and the IBC-PB composites. To do this, we conducted an MTT assay using RAW 264.7 macrophage cells (Fig. 7a). The PB NPs demonstrated an increasing toxic effect as the PB concentration was increased. The PB NPs started to show cell viability of less than 72% at a PB concentration of 50 μg mL^{-1} and showed cell viability of 19% at a concentration of 2500 μg mL^{-1}. Meanwhile, the IBC-PB composites showed no noticeable cytotoxic effect up to 2500 μg mL^{-1}, and the viability of IBC-PB composites-treated cells was 4.4-fold higher than that of PB NPs-treated cells at that concentration. It was clear that IBC-PB composites were far less toxic than

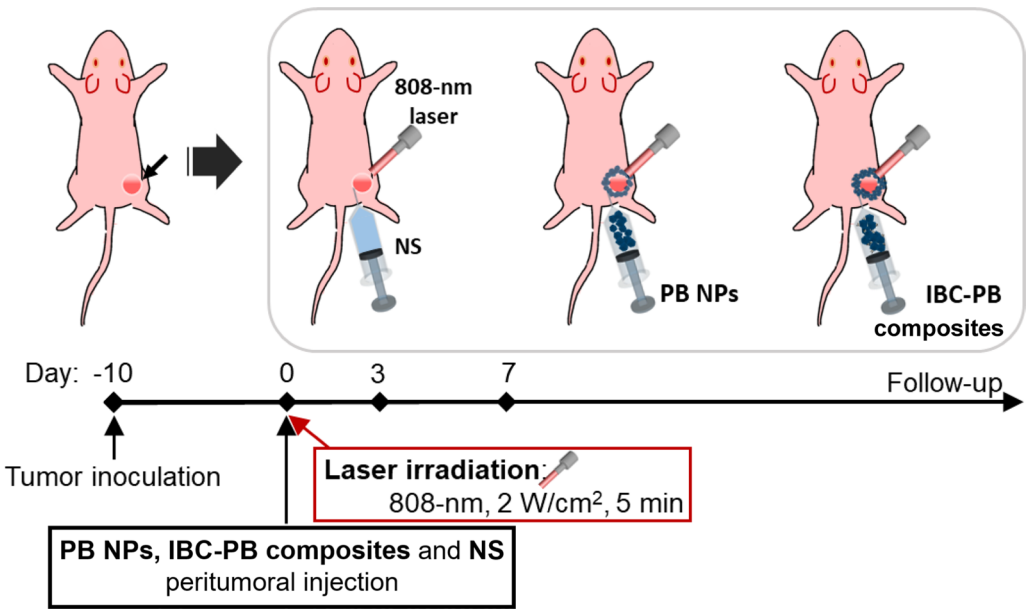

Fig. 5 Experimental design of IBC-PB composites-mediated in vivo PTT

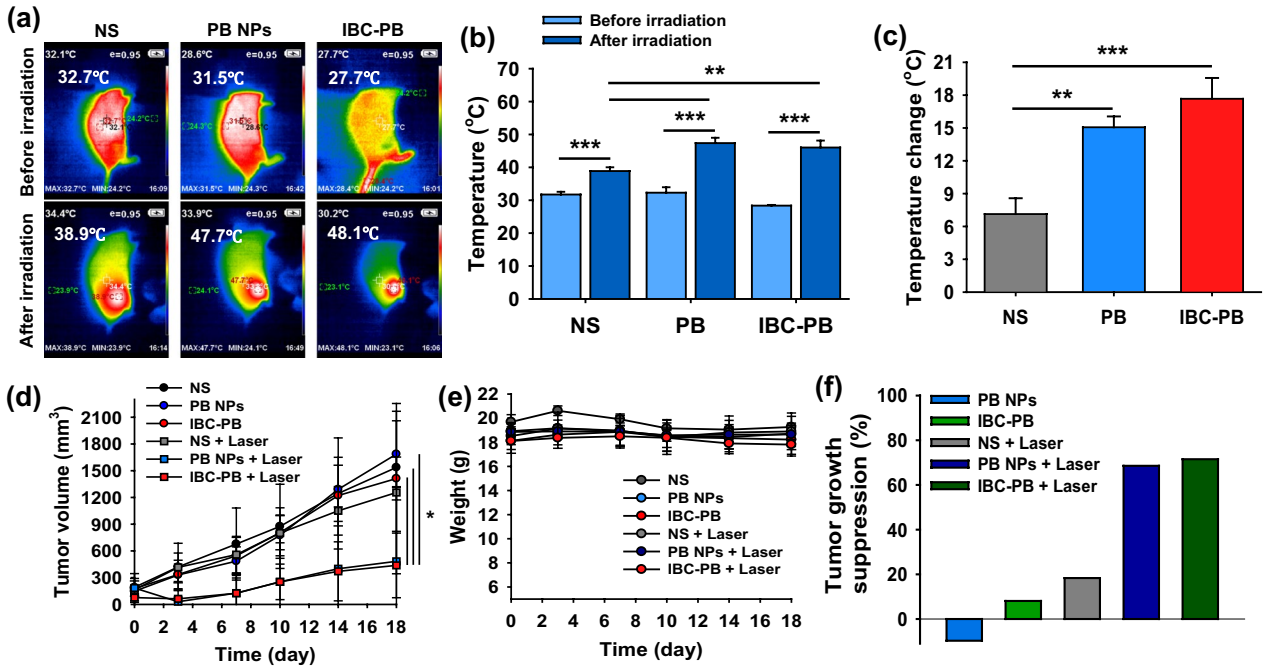

Fig. 6 In vivo photothermal imaging and PTT study: **a** in vivo photothermal imaging with NS, PB NPs, and IBC-PB composites in a 4T1 tumor bearing Balb/c nude mouse model. **b** Temperature changes in the tumor regions after laser irradiation (808-nm, 2 W cm^{-2}, 5 min) of NS, PB NPs, and IBC-PB composites (n = 3, mean ± s.d.). **c** Temperature increases at the tumor regions before and after laser irradiation of NS, PB NPs, and IBC-PB composites (n = 3, mean ± s.d.). **d** Tumor volume and (**e**) body weight profiles of 4T1 tumor-bearing mice after PTT (808 nm, 2 W cm^{-2}, 5 min) peritumorally injected with NS, PB NPs, and IBC-PB composites (n = 3, mean ± s.d.). **f** Tumor growth suppression ratio 18 days after follow-up based on tumor volume measurements. *: P < 0.05, **: P < 0.01, ***: P < 0.001. The statistical analysis was conducted by means of a student's t test for b, c, and d. (*IBC-PB* IBC-PB composites)

PB NPs in RAW 264.7 macrophage cells. We also measured the in vitro therapeutic window (Fig. 7b) based on the cell viability presented in Figs. 4c, d, 7a. We defined the in vitro therapeutic window as a concentration range from the concentration at which 50% of cancer cells survived with laser irradiation (therapeutic dose) to the concentration at which 80% of macrophage cells survived without laser irradiation (non-toxic dose) (Additional file 1: Fig S5). It should be noted that IBC-PB composites showed 84% cell viability even at the highest dose (2500 μg mL^{-1}); accordingly, 2500 μg mL^{-1} was considered as a non-toxic dose of IBC-PB composites. We found that the in vitro therapeutic window for PB-NPs ranges from 76.7 to 97.7 ug ml^{-1}, while for IBC-PB composites, it ranges from 72.7 to 2500 ug ml^{-1}. Also, we defined the therapeutic index (TI) as the ratio between the therapeutic dose and non-toxic dose. The TIs for the PB-NPs and IBC-PB composites were 1.3 and 34.4, respectively.

In vivo toxicity test

The biocompatibilities of the IBC-PB composites and PB NPs were assessed through a biochemical analysis 24 h after the subcutaneous injection in the right thighs and a blood draw of normal Balb/c-nude mice (n = 3) (Fig. 7c). The NS group served as a control group. The biocompatibility in each group was evaluated according to BUN, Cr, ALT, and AST, which are representative indicators of the kidney and liver function, respectively. In the BUN and Cr indices, the PB NPs and IBC-PB composites groups showed little difference numerically when compared with the NS group. The IBC-PB composites showed no significant difference compared to the NS group in terms of ALT and AST. However, in the PB NPs group, ALT was 1.30-fold higher and AST was 1.61-fold higher compared to that of the IBC-PB composites. The H&E-stained tissues from major organs (heart, liver, spleen, and kidney) in each group were imaged to confirm systemic toxicity (Fig. 7d). There were no significant signs of damage in any of the major organs, including the livers of the NS and IBC-PB composites groups. Meanwhile, prominent hepatocytic vacuolation was observed in the liver image of the PB NPs group, indicating acute liver toxicity [59, 60], unlike the liver tissue images of the other two groups. We speculate that for the IBC-PB composites, PB NPs were directly bound to BC, remaining at the injection site and not affecting the body, whereas the PB NPs were absorbed into the body 24 h after the injection and affected the liver function, leading to acute liver damage.

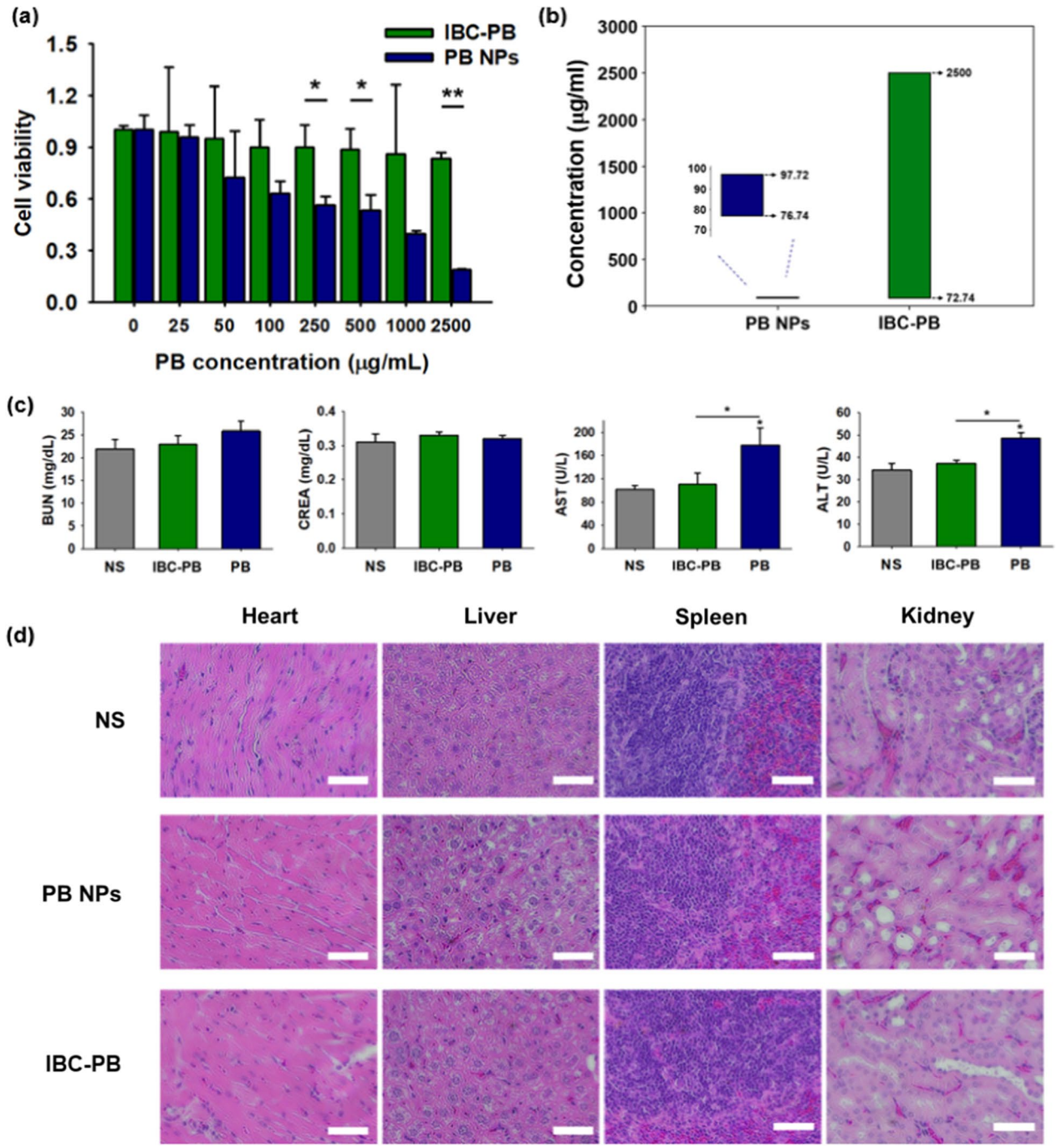

Fig. 7 Cytotoxicity and systemic toxicity effect of the IBC-PB composites: (**a**) in vitro cytotoxic effect comparison between the IBC-PB composites and the PB NPs in the RAW 264.7 cell line (n = 3, mean ± s.d.). **b** In vitro therapeutic window of the PB NPs and IBC-PB composites. **c** Biochemical analysis of blood 24 h after a subcutaneous injection of the NS, PB NPs, and IBC-PB composites into mice (kidney function indices: blood urea nitrogen (BUN) and creatine (CREA), liver function indices: aspartate transaminase (AST) and alanine transaminase (ALT)) (n = 3, mean ± s.d.). **d** H&E staining paraffin-sectioned images of major organs 24 h after a subcutaneous injection of NS, PB NPs, and IBC-PB composites in mice. *: $P < 0.05$, **: $P < 0.01$, ***: $P < 0.001$. The statistical analysis was conducted by means of a student's t test for a and b. (IBC-PB: IBC-PB composites)

Several studies have described the use of engineered PB NPs to achieve efficient PTT effects, theranostic properties, or improved biocompatibility. Wang et al. describes the development of a boracic-acid-modified graphite carbon nitride and PB nanohybrid for theranostic applications, offering targeted Raman recognition and

synergistic photothermal/photodynamic therapy in the near-infrared region [27]. A NaDyF4:50%Lu@PB nanocomposite was developed by Liu et al. as a biocompatible and effective PTT agent, which also possesses the ability to be used for magnetic resonance imaging [29]. Jing et al. developed a multifunctional nanoplatform by modifying hollow PB NPs with hyaluronic acid grafting polyethylene glycol and loaded with 10-hydroxycamptothecin for tumor-specific thermochemotherapy [61]. Chen et al. developed PEGylated PB NPs loaded with doxorubicin as a photothermal-chemo therapy for cancer [62]. Due to variations in therapeutic techniques, such as differences in laser settings and the use of additional therapeutic agents, it is challenging to make direct comparisons of therapeutic effects across studies. However, we were able to evaluate and compare the safety profile of the nanocomposites here, as presented in Table 1. Of the PB-containing nanocomposites, our IBC-PB composites exhibited the most biocompatible profile.

Various routes have been investigated for the administration of therapeutic nanoparticles, including intravenous, intramuscular, subcutaneous, intralesional, and perilesional types [63]. Among these routes, the localized administration of nanoparticles through intramuscular, subcutaneous, intralesional, and perilesional routes has been deemed ineffective for treating cancer due to the disseminating nature of cancer. However, several studies of cancer therapies based on locally injectable PB NPs have been reported, showing synergistic therapeutic effects when combined with other therapy strategies such as chemotherapy, radiotherapy, and immunotherapy. A gellan-based nanocomposite (NC) hydrogel embedding combretastatin A4 (CA4), a tubulin polymerization inhibitor for tumor growth suppression in cancer chemotherapy, and PB NPs showed a strong synergistic therapeutic effect as a type of NIR-triggered PTT and disrupting tumor vascular due to the continuous release of the CA4 [64]. An injectable PB-NPs-encapsulated agarose hydrogel, termed a PB reservoir and release controller (PRC) nanosystem, functioned as an improved combination therapy with PTT and radiotherapy (RT) given its excellent photothermal characteristics upon 808 nm NIR laser irradiation and with the catalytic capabilities of a radiosensitizer by converting endogenous hydrogen peroxide into oxygen for reactive oxygen species production by X-ray mediated RT [65]. A localized therapy using nanoparticles was also found to improve the efficacy of immunotherapy significantly, as the destruction of cancer cells in the nanoparticle-mediated therapy results in a release of cancer antigens, which in turn stimulates the adaptive immune system [66]. Juliana et al. used photothermal immunotherapy to enhance an immunotherapeutic effect with anti-cytotoxic T-lymphocyte antigen-4 (CTLA-4), well known as an immune checkpoint inhibitor (ICI), by means of PTT based on pH-dependent and intratumorally injectable PB NPs [67]. The studies discussed above suggest that IBC-PB composites could have broader applications, including disseminated cancer treatments, when used in combination with other cancer therapy systems, particularly immunotherapy.

Conclusion

We developed a highly biocompatible, repeatable PTT agent by directly growing PB NPs on BC with a simple thermal reduction process. The synthesized IBC-PB composites had a monodispersed PB-NP-decorated BC morphology, a strong hyperthermal effect, an excellent PTT effect, and good recyclability. The IBC-PB composites showed a PTT effect similar to that of PB NPs but with a considerably higher safety profile compared to PB NPs. Consequently, the IBC-PB composites developed here is a promising nanomaterial based on PB that can function as a highly biocompatible and repeatable PTT agent.

Table 1 Viability of cells treated with various forms of PB NPs

Particle name	Method	Cell viability at a certain concentration	Ref.
PB@Bg-C_3N_4	In situ reduction	95.6% at 200 μg mL^{-1}	[27]
$NaDyF_4$:50%Lu@PB	Solvothermal method	86% at 1000 μg mL^{-1}	[29]
HCPT@HPBNs@PAA/PAH/HA-g-PEG	Self-etching reaction and PEGylation by ECD-NHS reaction	56% at 30 μg mL^{-1}	[61]
PEGylated PB NPs	Precipitation, thin film hydration method	84.2% at 40 μg mL^{-1}	[62]
IBC-PB composites	Trituration and self-etching reaction	83.59% at 2500 μg mL^{-1}	Our study

PB@ Bg-C_3N_4 a boracic-acid-modified graphite carbon nitride and Prussian blue nanohybrid, *HCPT@HPBNs@PAA/PAH/HA-g-PEG* 10-hydroxycamptothecin loaded hyaluronic acid grafting polyethylene glycol modified hollow Prussian blue nanoparticles, *$NaDyF_4$:50%Lu@PB* Prussian blue-coated $NaDyF_4$ doped with Lu^{3+} ions nanocomposites, *PEGylated PB NPs* polyethylene glycol-attached Prussian blue nanoparticles

Experimental section

Materials

Bacterial cellulose (nata de coco) was obtained from Vietnam Coco Food Co., Ltd. (Tang Nhon Phu, Vietnam). Potassium ferricyanide trihydrate ($K_3[Fe(CN)_6]\cdot 3H_2O$), thiazolyl blue tetrazolium bromide, and Roswell Park Memorial Institute (RPMI) 1640 were obtained from Sigma-Aldrich (St. Louis, MO, USA). $Cu(OH)_2$ was purchased from Alfa Aesar (Haverhill, MA, USA). The ammonia solution, sodium hydroxide (NaOH), hydrochloric acid (HCl), and diethyl ether used here were purchased from Samchun (Gangnam, Korea). Polyvinylpyrrolidone (PVP, K30) was purchased from Kanto Chemical Co. (Tokyo, Japan). Fetal bovine serum (FBS) was purchased from GE Healthcare Life Sciences (Buckinghamshire, UK), and 4% paraformaldehyde (PFA) was obtained from Biosesang (Seongnam, Korea) to fix the major organs. Female Balb/c nude mice (6–8 weeks) were purchased from Orient Bio (Seongnam, Korea) for the in vivo PTT experiment. The BD vacutainer® SST™ system used in the study was purchased from BD Bioscience (New Jersey, USA).

Preparation of PB NPs

PB NPs were synthesized according to a method reported in the literature [68]. PVP K30 (3 g) and $K_3[Fe(CN)_6]$ (132 mg) were dissolved in a HCl solution (0.01 M, 40 mL) under vigorous magnetic stirring. After 30 min of stirring, a clear yellow solution was obtained, which was then placed in an oven at 80 ℃ for 24 h. The precipitates were collected by centrifugation and washed in distilled water, ethanol, and diethyl ether at 8000 rpm for 20 min several times. After drying at 60 ℃ in an oven for 24 h, PB nanoparticle powder was obtained.

Synthesis of IBC

The impurities of nata de coco (1 kg) were removed by dialysis with deionized water (D.W.) for three days. After the washing process, the nata de coco was physically pulverized through a grinder and filtered through a sieve several times. Water was completely removed from the physically treated nata de coco through freeze-drying for more than 4 days. Schweitzer's reagent was produced by dissolving copper hydroxide (100 mg) in an ammonia solution (5 ml) and stirring sufficiently. Lyophilized nata de coco (50 mg) was added to Schweitzer's reagent (5 ml) and reacted for two hours at room temperature under vigorous stirring. Subsequently, mixture of Schweitzer's reagent and bacterial cellulose was added to 20 ml of a 10% HCl solution for neutralization and the mixture was stirred sufficiently until the color no longer changed. The neutralized bacterial cellulose was filtered by a glass filter and washed with D.W. several times until the pH reached approximately 7. After washing, the collected bacterial cellulose was dispersed in D.W. (20 ml) and stored in a refrigerator at 5 ℃.

Synthesis of IBC-PB composites

In 20 ml of the IBC solution, D.W. (70 ml), 1 M HCl (10 ml) and $K_3[Fe(CN)_6]\cdot 3H_2O$ (0.25 mmol, 0.5 mmol, 0.75 mmol, 1 mmol) were added, reaching a total solution amount of 100 ml. This mixture was reacted for 24 h at 80 ℃ oven. The IBC-PB composites were collected by filtration with a glass filter and washed with D.W. several times until the pH was approximately 7. After washing, the collected IBC-PB composites were dispersed in 50 ml D.W. and stored in a refrigerator at 5 ℃.

Characterization of IBC-PB composites

The produced composites were characterized using a field-emission scanning electron microscope (FE-SEM, Hitachi S-4800). The crystal structure of the composites was confirmed by a powder X-ray diffraction analysis using a Bruker D8 Advance device (Cu Ka1 radiation, $5°min^{-1}$). A thermogravimetric analysis (TGA) was conducted using a TGA/DSC 1 analyzer (Mettler Toledo) with a heating rate of 5 ℃ min^{-1} in air. An inductively coupled plasma atomic emission spectroscopy (ICP-AES) analysis was conducted in 6000 K Ar plasma with a range of 167–782 nm (OPTIMA 8300, Perkin-Elmer, USA). The absorbance was measured by a microplate reader (SYNERGY H1, BioTek, Winooski, VT, USA). An 808 nm NIR laser (FC-W-808-10W, CNI, Changchun, China) was used for photothermal imaging and PTT studies. A thermal imaging camera (HT-18, HT Instruments, Faenza, Italy) was used for real-time hyperthermal imaging. A blood biochemistry analyzer (Hitachi 7020, Tokyo, Japan) was utilized for the blood biochemical analysis. A Nicolet5700 FTIR spectrometer (Thermo electron Corporation, United States) with a measurement range of 4000–400 cm^{-1} was used to record the infrared spectra.

Photothermal performance test

The IBC-PB composites (0.2 mg 1.5 ml^{-1}) dispersed in D.W. was added to a 4 ml vial, a stirring bar was added, and the surroundings were wrapped with Styrofoam. An 808 nm NIR laser (1 W cm^{-2}) was irradiated 5 mins onto each sample and the temperature was measured every 30 s. According to the experimental results, we collected the best sample, and it was used for a retention test. The retention test was conducted by repeating the 5 min laser irradiation, which was followed by cooling to the initial temperature 5 times.

The evaluation of in vitro cytotoxicity and photothermal therapeutic effect

4T1 breast cancer cell and RAW 264.7 macrophage cell lines were authenticated and obtained from the Korean Cell Line Bank, Korea). The cells were cultured, added to a 96-well microplate (10^3 cells 200 μL^{-1} of RPMI 1640 or DMEM), and incubated at 37 ℃ with 5% CO_2 for 24 h. After incubation, the cell media were discarded and the cells were washed with DPBS three times to remove remained media, followed by an exchange for new cell media in each well. The PB NPs and IBC-PB composites were incubated with RAW 264.7 cells with PB concentration gradients (0, 25, 50, 100, 250, 500, 1000, and 2500 μg mL^{-1}). The BC and IBC-PB composites were added to the 4T1 cancer cells with the series of BC concentrations (0, 10, 50, 100, 200, and 500 μg mL^{-1}). All nanomaterial treated cells were incubated overnight. The IBC-PB composite-treated 4T1 cells were irradiated with an 808-nm laser at 2 W cm^{-2} for five minutes and another 24 h of incubation was conducted. Subsequently, 0.5 mg mL^{-1} of MTT solution was added to each well after incubation and a DPBS washing step for two hours for the MTT assay. After the incubation of the MTT solution, cell images were obtained by an optical microscope of the IBC-PB composite-treated groups before the DMSO solvent exchange step. Each well was measured at 540 nm by the microplate reader to acquire its absorbance. Cell viability was calculated at a ratio relative to untreated control samples and the data were evaluated by a t-test. In vitro cytotoxicity test was carried out in triplicate.

Preparation of the 4T1 tumor-bearing mouse model

The 4T1 cancer cells were cultured and collected with PBS (10^5 cells 15 μL^{-1} PBS). The condensed 4T1 cells were injected subcutaneously into the right thigh of female Balb/c nude mouse. Further in vivo experiments with the mouse tumor model were performed when the tumor size reached approximately 50–100 mm^3. All animal studies were approved by the Institutional Animal Care and Use Committee of Woojung Bio Inc.

In vivo photothermal imaging

Normal saline (NS), the PB NPs, and the IBC-PB composites were used for a peritumoral injection (p.i.) at the tumor region in the 4T1 tumor bearing mice. After each injection, an 808 nm laser was irradiated at 2 W cm^{-2} for 5 mins, in vivo photothermal imaging was conducted, and photothermal images were obtained in each group during laser irradiation.

In vivo photothermal therapy study

First of all, the mice were randomized into three groups. The NS, PB NPs, and IBC-PB composites underwent a p.i. procedure around the tumor region in the 4T1 tumor bearing mice (n = 3). The 808 nm laser was irradiated under a condition identical to that used for the in vivo photothermal imaging step after the injection. The treated and untreated groups underwent a follow-up assessment for 18 days that involved measuring the tumor sizes and weights. The data were evaluated statistically by an ANOVA test.

The assessment for tumor retention of in vivo PB NPs and IBC-PB composites

The PB NPs and IBC-PB composites were inserted by peritumoral injection at the 4T1 tumor region. Photographic images were obtained at various time points post injection (0, 1, and 7 days). The tumor tissues were resectioned and internal photographic images were obtained.

Biocompatibility test of IBC-PB composite and PB NPs

The NS, PB NPs, and IBC-PB composites were subcutaneously injected into the right thigh region in each case. Blood samples with a volume of 500 μL were collected with a SST vacutainer in each group 24 h after the injection. The obtained blood samples were centrifuged, and the supernatant was re-collected for each sample. The supernatant was analyzed for indices that represent liver and kidney functions (alanine transaminase (ALT), aspartate transaminase (AST), creatinine (Cr), and blood urea nitrogen (BUN)) by a blood biochemistry analyzer. After the blood draw, major organs in each group were collected, stored in a 4% PFA solution, stained with hematoxylin and eosin (H&E) staining, and paraffin-sectioned for tissue imaging.

Supplementary Information

The online version contains supplementary material available at https://doi.org/10.1186/s12951-023-02108-6.

Additional file 1: Figure S1. SEM image of the bacterial cellulose (BC) to verify the morphology and structure. **Figure S2.** SEM image of the PB NPs to verify the size and morphology. **FigureS3.** FTIR spectra for BC and IBC-PB composites. **Figure S4.** Photographic images of in vivo retention ability comparison between PB NPs and IBC-PB composites at different time points (0, 1, 7 days). White circle indicate the peritumoral injected IBC-PB composites. **Figure S5.** In vitro therapeutic window determination of PB NPs and IBC-PB composites. (a) therapeutic dose and (b) non-toxic dose of PB NPs, and (c) therapeutic dose and (d) non-toxic dose of IBC-PB composites.

Acknowledgements

This research was supported by grants funded by the National Research Foundation of Korea (NRF) (NRF-2019M2D2A1A01058210, NRF-2020R1C1C1009000, NRF-2021M2E8A1039564, NRF-2022R1A6A1Ă3039); by a grant from the Korea Evaluation Institute of Industrial Technology (KEIT) funded by the Korean government (MOTIE) (No. 20018522); and by the Korea Drug Development

Fund funded by the Ministry of Science and ICT, Ministry of Trade, Industry and Energy and the Ministry of Health and Welfare (HN22C0632) of Korea. Schematic illustrations were created with BioRender.

Author contributions
First of all, Yuanzhe Piao and Hyung-Jun Im are corresponding authors. Hwichan Hong: Conceptualization - equal / Data curation - lead / Writing original draft - equal / Writing review&editing - supporting / Formal analysis - equal / Investigation - lead / Revision - lead MinKyu Kim: Data curation - equal / Writing original draft - equal / Writing review&editing - lead / Formal analysis - supporting / Investigation - equal / Revision - lead Wooseung Lee: Writing original draft - equal / Formal analysis - equal / Investigation - supporting Miyeon Jeon: Formal analysis - supporting Chaedong Lee: Conceptualization - equal / Investigation - supporting Hoonsub Kim: Formal analysis - supporting Hyung-Jun Im and Yuanzhe Piao: Supervising and Project administration Hwichan Hong prepared figures 1, 2, S1, and S2. MinKyu Kim prepared Graphical abstracts, figure 7, S4, and table 1. Wooseung Lee prepared figures 3-6, and S3.

Data availability
The datasets used and/or analysed during the current study available from the corresponding author on reasonable request.

Declarations

Ethics approval and consent to participate
All animal experiments were approved by the Institutional Animal Care and Use Committee of Woojung Bio Inc.

Competing interests
Hyung-Jun Im is the co-founder and the Chief Scientific Officer of Portrai. The authors declare that they have no competing interests.

Author details
[1]Department of Applied Bioengineering, Graduate School of Convergence Science and Technology, Seoul National University, Seoul 08826, Republic of Korea. [2]Department of Molecular Medicine and Biopharmaceutical Sciences, Graduate School of Convergence Science and Technology, Seoul National University, Seoul 08826, Republic of Korea. [3]Cancer Research Institute, Seoul National University, Seoul 03080, Republic of Korea. [4]Advanced Institutes of Convergence Technology, Seoul National University, Suwon-si, Gyeonggi-do, Republic of Korea. [5]Research Institute for Convergence Science, Seoul National University, Seoul, Republic of Korea.

Received: 2 June 2023 Accepted: 15 September 2023
Published online: 05 October 2023

References

1. Li X, Lovell JF, Yoon J, Chen X. Clinical development and potential of photothermal and photodynamic therapies for cancer. Nat Rev Clin Oncol. 2020;17(11):657–74.
2. Liu S, Pan X, Liu H. Two-dimensional nanomaterials for photothermal therapy. Angew Chem. 2020;132(15):5943–53.
3. Jung HS, Verwilst P, Sharma A, Shin J, Sessler JL, Kim JS. Organic molecule-based photothermal agents: an expanding photothermal therapy universe. Chem Soc Rev. 2018;47(7):2280–97.
4. Liu Y, Bhattarai P, Dai Z, Chen X. Photothermal therapy and photoacoustic imaging via nanotheranostics in fighting cancer. Chem Soc Rev. 2019;48(7):2053–108.
5. Huang X, El-Sayed IH, Qian W, El-Sayed MA. Cancer cell imaging and photothermal therapy in the near-infrared region by using gold nanorods. J Am Chem Soc. 2006;128(6):2115–20.
6. Melamed JR, Edelstein RS, Day ES. Elucidating the fundamental mechanisms of cell death triggered by photothermal therapy. ACS Nano. 2015;9(1):6–11.
7. Pérez-Hernández M, Del Pino P, Mitchell SG, Moros M, Stepien G, Pelaz B, Parak WJ, Gálvez EM, Pardo J, de la Fuente JM. Dissecting the molecular mechanism of apoptosis during photothermal therapy using gold nanoprisms. ACS Nano. 2015;9(1):52–61.
8. Li J, Zhang W, Ji W, Wang J, Wang N, Wu W, Wu Q, Hou X, Hu W, Li L. Near infrared photothermal conversion materials: mechanism, preparation and photothermal cancer therapy applications. J Mater Chem B. 2021. https://doi.org/10.1039/D1TB01310F.
9. Lan M, Zhao S, Zhang Z, Yan L, Guo L, Niu G, Zhang J, Zhao J, Zhang H, Wang P. Two-photon-excited near-infrared emissive carbon dots as multifunctional agents for fluorescence imaging and photothermal therapy. Nano Res. 2017;10(9):3113–23.
10. Zhou F, Da X, Ou Z, Wu B, Resasco DE, Chen WR. Cancer photothermal therapy in the near-infrared region by using single-walled carbon nanotubes. J Biomed Opt. 2009;14(2):021009.
11. Kang B, Mackey MA, El-Sayed MA. Nuclear targeting of gold nanoparticles in cancer cells induces DNA damage, causing cytokinesis arrest and apoptosis. J Am Chem Soc. 2010;132(5):1517–9.
12. Kim D, Jeong YY, Jon S. A drug-loaded aptamer– gold nanoparticle bioconjugate for combined CT imaging and therapy of prostate cancer. ACS Nano. 2010;4(7):3689–96.
13. Huang X, Jain PK, El-Sayed IH, El-Sayed MA. Plasmonic photothermal therapy (PPTT) using gold nanoparticles. Lasers Med Sci. 2008;23(3):217–28.
14. Boca-Farcau S, Potara M, Simon T, Juhem A, Baldeck P, Astilean S. Folic acid-conjugated, SERS-labeled silver nanotriangles for multimodal detection and targeted photothermal treatment on human ovarian cancer cells. Mol Pharm. 2014;11(2):391–9.
15. Wang Z, Chang Z, Lu M, Shao D, Yue J, Yang D, Li M, Dong W-F. Janus silver/silica nanoplatforms for light-activated liver cancer chemo/photothermal therapy. ACS Appl Mater Interfaces. 2017;9(36):30306–17.
16. Bian K, Zhang X, Liu K, Yin T, Liu H, Niu K, Cao W, Gao D. Peptide-directed hierarchical mineralized silver nanocages for anti-tumor photothermal therapy. ACS Sustain Chem Eng. 2018;6(6):7574–88.
17. Tian Q, Hu J, Zhu Y, Zou R, Chen Z, Yang S, Li R, Su Q, Han Y, Liu X. Sub-10 nm Fe3O4@ Cu2–x S core–shell nanoparticles for dual-modal imaging and photothermal therapy. J Am Chem Soc. 2013;135(23):8571–7.
18. Estelrich J, Busquets MA. Iron oxide nanoparticles in photothermal therapy. Molecules. 2018;23(7):1567.
19. Lambert TN, Andrews NL, Gerung H, Boyle TJ, Oliver JM, Wilson BS, Han SM. Water-soluble germanium (0) nanocrystals: cell recognition and near-infrared photothermal conversion properties. Small. 2007;3(4):691–9.
20. Sun W, Zhong G, Kübel C, Jelle AA, Qian C, Wang L, Ebrahimi M, Reyes LM, Helmy AS, Ozin GA. Size-tunable photothermal germanium nanocrystals. Angew Chem Int Ed. 2017;56(22):6329–34.
21. Rastinehad AR, Anastos H, Wajswol E, Winoker JS, Sfakianos JP, Doppalapudi SK, Carrick MR, Knauer CJ, Taouli B, Lewis SC. Gold nanoshell-localized photothermal ablation of prostate tumors in a clinical pilot device study. Proc Natl Acad Sci. 2019;116(37):18590–6.
22. Cheng Z, Al Zaki A, Hui JZ, Muzykantov VR, Tsourkas A. Multifunctional nanoparticles: cost versus benefit of adding targeting and imaging capabilities. Science. 2012;338(6109):903–10.
23. Hoffman HA, Chakrabarti L, Dumont MF, Sandler AD, Fernandes R. Prussian blue nanoparticles for laser-induced photothermal therapy of tumors. RSC Adv. 2014;4(56):29729–34.
24. Fu G, Liu W, Feng S, Yue X. Prussian blue nanoparticles operate as a new generation of photothermal ablation agents for cancer therapy. Chem Commun. 2012;48(94):11567–9.
25. Cheng L, Gong H, Zhu W, Liu J, Wang X, Liu G, Liu Z. PEGylated prussian blue nanocubes as a theranostic agent for simultaneous cancer imaging and photothermal therapy. Biomaterials. 2014;35(37):9844–52.
26. Jing L, Liang X, Deng Z, Feng S, Li X, Huang M, Li C, Dai Z. Prussian blue coated gold nanoparticles for simultaneous photoacoustic/CT bimodal imaging and photothermal ablation of cancer. Biomaterials. 2014;35(22):5814–21.
27. Wang Y-N, Zhang W-S, Liu X-P, Wei Y-Y, Xu Z-R. A nanohybrid of Prussian blue supported by boracic acid-modified g-C3N4 for Raman recognition of cell surface sialic acid and photothermal/photodynamic therapy. Colloids Surf, B. 2022;215:112490.
28. Long J, Guari Y, Guérin C, Larionova J. Prussian blue type nanoparticles for biomedical applications. Dalton Trans. 2016;45(44):17581–7.
29. Liu Y, Guo Q, Zhu X, Feng W, Wang L, Ma L, Zhang G, Zhou J, Li F. Optimization of prussian blue coated NaDyF4: x% Lu nanocomposites for

multifunctional imaging-guided photothermal therapy. Adv Func Mater. 2016;26(28):5120–30.
30. Patra CR. Prussian blue nanoparticles and their analogues for application to cancer theranostics. Future Med. 2016;11:569–72.
31. Fu J, Wu B, Wei M, Huang Y, Zhou Y, Zhang Q, Du L. Prussian blue nanosphere-embedded in situ hydrogel for photothermal therapy by peritumoral administration. Acta Pharmaceutica Sinica B. 2019;9(3):604–14.
32. Chen Y, Wu L, Wang Q, Wu M, Xu B, Liu X, Liu J. Toxicological evaluation of prussian blue nanoparticles after short exposure of mice. Hum Exp Toxicol. 2016;35(10):1123–32.
33. Hu W, Chen S, Liu L, Ding B, Wang H. Formaldehyde sensors based on nanofibrous polyethyleneimine/bacterial cellulose membranes coated quartz crystal microbalance. Sens Actuators, B Chem. 2011;157(2):554–9.
34. Pourreza N, Golmohammadi H, Naghdi T, Yousefi H. Green in-situ synthesized silver nanoparticles embedded in bacterial cellulose nanopaper as a bionanocomposite plasmonic sensor. Biosens Bioelectron. 2015;74:353–9.
35. Torgbo S, Sukyai P. Bacterial cellulose-based scaffold materials for bone tissue engineering. Appl Mater Today. 2018;11:34–49.
36. Almeida I, Pereira T, Silva N, Gomes F, Silvestre A, Freire C, Lobo JS, Costa P. Bacterial cellulose membranes as drug delivery systems: an in vivo skin compatibility study. Eur J Pharm Biopharm. 2014;86(3):332–6.
37. Amin MCIM, Ahmad N, Halib N, Ahmad I. Synthesis and characterization of thermo-and pH-responsive bacterial cellulose/acrylic acid hydrogels for drug delivery. Carbohyd Polym. 2012;88(2):465–73.
38. Trovatti E, Freire CS, Pinto PC, Almeida IF, Costa P, Silvestre AJ, Neto CP, Rosado C. Bacterial cellulose membranes applied in topical and transdermal delivery of lidocaine hydrochloride and ibuprofen: in vitro diffusion studies. Int J Pharm. 2012;435(1):83–7.
39. Maneerung T, Tokura S, Rujiravanit R. Impregnation of silver nanoparticles into bacterial cellulose for antimicrobial wound dressing. Carbohyd Polym. 2008;72(1):43–51.
40. Wu J, Zheng Y, Song W, Luan J, Wen X, Wu Z, Chen X, Wang Q, Guo S. In situ synthesis of silver-nanoparticles/bacterial cellulose composites for slow-released antimicrobial wound dressing. Carbohyd Polym. 2014;102:762–71.
41. Lin W-C, Lien C-C, Yeh H-J, Yu C-M, Hsu S-H. Bacterial cellulose and bacterial cellulose–chitosan membranes for wound dressing applications. Carbohyd Polym. 2013;94(1):603–11.
42. Qiu Y, Qiu L, Cui J, Wei Q. Bacterial cellulose and bacterial cellulose-vaccarin membranes for wound healing. Mater Sci Eng, C. 2016;59:303–9.
43. Markstedt K, Mantas A, Tournier I, Martínez Ávila H, Hagg D, Gatenholm P. 3D bioprinting human chondrocytes with nanocellulose–alginate bioink for cartilage tissue engineering applications. Biomacromol. 2015;16(5):1489–96.
44. Africa TK. The production of nata from coconut water. Unitas. 1949;22:60–100.
45. Chiaoprakobkij N, Suwanmajo T, Sanchavanakit N, Phisalaphong M. Curcumin-loaded bacterial cellulose/alginate/gelatin as a multifunctional biopolymer composite film. Molecules. 2020;25(17):3800.
46. Barud HS, Souza JL, Santos DB, Crespi MS, Ribeiro CA, Messaddeq Y, Ribeiro SJ. Bacterial cellulose/poly (3-hydroxybutyrate) composite membranes. Carbohyd Polym. 2011;83(3):1279–84.
47. Wang H, Shao Z, Bacher M, Liebner F, Rosenau T. Fluorescent cellulose aerogels containing covalently immobilized (ZnS) x (CuInS2) 1–x/ZnS (core/shell) quantum dots. Cellulose. 2013;20(6):3007–24.
48. Ngoensawat U, Parnsubsakul A, Kaitphaiboonwet S, Wutikhun T, Sapcharoenkun C, Pienpinijtham P, Ekgasit S. Luminescent nanohybrid of ZnO quantum dot and cellulose nanocrystal as anti-counterfeiting ink. Carbohyd Polym. 2021;262:117864.
49. Li X, Chen S, Hu W, Shi S, Shen W, Zhang X, Wang H. In situ synthesis of CdS nanoparticles on bacterial cellulose nanofibers. Carbohyd Polym. 2009;76(4):509–12.
50. Chanthiwong M, Mongkolthanaruk W, Eichhorn SJ, Pinitsoontorn S. Controlling the processing of co-precipitated magnetic bacterial cellulose/iron oxide nanocomposites. Mater Des. 2020;196:109148.
51. Park S, Park J, Jo I, Cho S-P, Sung D, Ryu S, Park M, Min K-A, Kim J, Hong S. In situ hybridization of carbon nanotubes with bacterial cellulose for three-dimensional hybrid bioscaffolds. Biomaterials. 2015;58:93–102.
52. Yao J, Ji P, Sheng N, Guan F, Zhang M, Wang B, Chen S, Wang H. Hierarchical core-sheath polypyrrole@ carbon nanotube/bacterial cellulose macrofibers with high electrochemical performance for all-solid-state supercapacitors. Electrochim Acta. 2018;283:1578–88.
53. He F, Zhao D. Manipulating the size and dispersibility of zerovalent iron nanoparticles by use of carboxymethyl cellulose stabilizers. Environ Sci Technol. 2007;41(17):6216–21.
54. Zhu C, Jiang J, Jia Y, Xu ZP, Zhang L. Beyond drug delivery system: immunomodulatory layered double hydroxide nanoadjuvants take an essential step forward in cancer immunotherapy. Acc Mater Res. 2023. https://doi.org/10.1021/accountsmr.3c00094.
55. Wang H, Najibi AJ, Sobral MC, Seo BR, Lee JY, Wu D, Li AW, Verbeke CS, Mooney DJ. Biomaterial-based scaffold for in situ chemo-immunotherapy to treat poorly immunogenic tumors. Nat Commun. 2020;11(1):5696.
56. Wang C, Sun Z, Zhao C, Zhang Z, Wang H, Liu Y, Guo Y, Zhang B, Gu L, Yu Y. Maintaining manganese in tumor to activate cGAS-STING pathway evokes a robust abscopal anti-tumor effect. J Control Release. 2021;331:480–90.
57. Wang Y, Wang Z, Chen B, Yin Q, Pan M, Xia H, Zhang B, Yan Y, Jiang Z, Zhang Q. Cooperative self-assembled nanoparticle induces sequential immunogenic cell death and toll-like receptor activation for synergistic chemo-immunotherapy. Nano Lett. 2021;21(10):4371–80.
58. Yang L, Lang Y, Wu H, Xiang K, Wang Y, Yu M, Liu Y, Yang B, He L, Lu G. Engineered toll-like receptor nanoagonist binding to extracellular matrix elicits safe and robust antitumor immunity. ACS Nano. 2023;17(6):5340–53.
59. Aref AM, Tohamy AA, Abdel Moneim AE, Sayed RH. Cinnamic acid attenuates cisplatin-induced hepatotoxicity and nephrotoxicity. 2016.
60. Nayak N, Sathar SA, Mughal S, Duttagupta S, Mathur M, Chopra P. The nature and significance of liver cell vacuolation following hepatocellular injury—an analysis based on observations on rats rendered tolerant to hepatotoxic damage. Virchows Arch. 1996;428(6):353–65.
61. Jing L, Wang Y, Yang Y, Yue X, Dai Z. Hyaluronic acid modified hollow Prussian blue nanoparticles loading 10-hydroxycamptothecin for targeting thermochemotherapy of cancer. Theranostics. 2016;6(1):40.
62. Chen H, Ma Y, Wang X, Wu X, Zha Z. Facile synthesis of Prussian blue nanoparticles as pH-responsive drug carriers for combined photothermal-chemo treatment of cancer. RSC Adv. 2017;7(1):248–55.
63. Mitchell MJ, Billingsley MM, Haley RM, Wechsler ME, Peppas NA, Langer R. Engineering precision nanoparticles for drug delivery. Nat Rev Drug Discovery. 2021;20(2):101–24.
64. Liang Y, Hao Y, Wu Y, Zhou Z, Li J, Sun X, Liu Y-N. Integrated hydrogel platform for programmed antitumor therapy based on near infrared-triggered hyperthermia and vascular disruption. ACS Appl Mater Interfaces. 2019;11(24):21381–90.
65. Wang Z, Zeng W, Chen Z, Suo W, Quan H, Tan Z-J. An intratumoral injectable nanozyme hydrogel for hypoxia-resistant thermoradiotherapy. Colloids Surf, B. 2021;207:112026.
66. Irvine DJ, Dane EL. Enhancing cancer immunotherapy with nanomedicine. Nat Rev Immunol. 2020;20(5):321–34.
67. Cano-Mejia J, Burga RA, Sweeney EE, Fisher JP, Bollard CM, Sandler AD, Cruz CRY, Fernandes R. Prussian blue nanoparticle-based photothermal therapy combined with checkpoint inhibition for photothermal immunotherapy of neuroblastoma. Nanomed Nanotechnol Biol Med. 2017;13(2):771–81.
68. Hu M, Furukawa S, Ohtani R, Sukegawa H, Nemoto Y, Reboul J, Kitagawa S, Yamauchi Y. Synthesis of prussian blue nanoparticles with a hollow interior by controlled chemical etching. Angew Chem Int Ed. 2012;51(4):984–8.

Publisher's Note